Highly Precise Magnetic Field Measurement Based RF-Assisted Sagnac Interferometer With Tapered Fiber

Sanfeng Gu, Danqi Feng, Yangxu Tang, Zhonghao Li, Xinhao Nan, Tianqi Wang, and Ming Deng

***Abstract*—A radio frequency (RF)-assisted Sagnac interferometer based on a dual-loop optoelectronic oscillator (OEO) is experimentally demonstrated for high-precision magnetic field measurement, in which the tapered fiber covered with the magnetic fluid (MF) as the magnetic field sensing head is embedded in the Sagnac interferometer. The evanescent field of the tapered fiber can interact with the MF under the external magnetic field to cause the birefringence variation of the fundamental mode, leading to the change in the free spectral range (FSR) of the interferometer, which can be mapped to the oscillation frequency shift of the OEO in the microwave domain. By the above converting, the magnetic field measurement with high interrogation speed and resolution can be realized. In addition, the designed device shows a certain measurement directionality of the magnetic field due to two orthogonally polarized fundamental modes asymmetric to the magnetic field, obtaining a good conformity with the constructed theoretical models. The experimental results show the maximum magnetic field sensitivities of 159.4 Hz/mT in the range of 8.48-27.83 mT, and 350.8 Hz/mT in the range of 0-5.14 mT, corresponding to the light wave vector parallel and perpendicular to the magnetic field, respectively.**

***Index Terms*—Magnetic field measurement, magnetic fluid, optoelectronic oscillator, sagnac interferometer.**

I. Introduction

MAGNETIC field measurement is of great significance in the scientific and industrial fields, such as fault diagnosis in power industry [1], geomagnetic detection [2], aviation industry [3], and biological magnetic measurement [4]. The magnetic fluid (MF) as a kind of functionalized magnetic material can generate satisfactory response to external magnetic field because of the excellent optical properties including linear/circular birefringence, dichroism, and refractive index (RI) tunability [5], [6], [7], [8]. Therefore, the fiber interferometers incorporating with MF are widely used for the magnetic field measurement due to the remarkable merits of high sensitivity, small size, flexible integration, remote distance interrogation, anti-electromagnetic interference, low cost and easy fabrication [9], [10], [11]. Especially, the MF-based Sagnac interferometers utilizing the birefringence property have been extensively studied due to the advantages of flexibly controlling the measurement sensitivity and free spectral range (FSR) of the transmission spectrum by changing the polarization maintaining fiber (PMF) length [12], [13]. For example, Lei et al. demonstrated a Sagnac loop with the MF-coated D-shaped microstructure prepared by a femtosecond laser, obtaining the spectral sensitivity of 82.3 pm/mT in the range of 0–30.4 mT [14]. Wei et al. utilized the MF-covered microfiber coupler to form a Sagnac loop, revealing the spectral sensitivity of -100 and -488 pm/mT with the PMF lengths of 75 and 20 cm, respectively [15]. In order to further improve the mode birefringence of the optical field to enhance the measurement sensitivity, the most direct way is to let the light field firsthand pass through the MF. Wang et al. verified a MF-filled hollow-core waveguide embedded in a Sagnac loop, achieving the wavelength sensitivity of 292 pm/mT in the range of 0-30 mT [16]. Zhang et al. proved a Sagnac interferometer with the MF-immersed asymmetric four-hole fiber (AFHF), showing the wavelength sensitivity of 2262 pm/mT in the range of 0.296–8.9 mT [17]. Although the above sensing heads have relatively compact size and high sensitivity, they increase the operation difficulty of the MF filling into the micro-structured fibers and the fusion difficulty at the same time. Moreover, it should be noted that the above mentioned sensors have something in common, that is, the magnetic field sensitivity is characterized by monitoring the wavelength shift in the spectrum analyzer. Therefore, there are two unavoidable drawbacks, where one is undoubtedly limited by the low resolution of the spectrometer ($\sim$20 pm), and the other is the relatively slow scanning speed of the spectrometer, which cannot synchronously follow the real-time and online sensing signals of the sensors. Alternatively, optoelectronic oscillator (OEO) interrogating the fiber interferometers as an effective way can convert the optical parameters (wavelength or FSR) change into the oscillation frequency shift in the microwave domain,

Manuscript received 14 October 2022; revised 6 December 2022; accepted 15 December 2022. Date of publication 19 December 2022; date of current version 29 December 2022. This work was supported in part by the National Natural Science Foundation of China under Grants 61905029 and 62075022, in part by the Graduate Research and Innovation Foundation of Chongqing, China under Grant CYB22059, in part by the Opening Foundation of the National Key Laboratory of Precision Testing and Instrumentation under Grant pilab 2204, in part by the Chongqing Technology Innovation and Development Project under Grant cstc2020jscx-msxmX0216, in part by the Chongqing National Science Foundation of Innovative Reach Groups under Grant cstc2020jcyj-cxttX0005, and in part by the Chongqing Human Resources and Social Security Bureau under Grant cx2020016. *(Corresponding author: Ming Deng.)*

The authors are with the Key Laboratory of Optoelectronic Technology and Systems (Ministry of Education), Chongqing University, Chongqing 400044, China (e-mail: gusf@cqu.edu.cn; fdq1228@cqu.edu.cn; 15235110996@163.com; 202108021059t@cqu.edu.cn; 202008021005@cqu.edu.cn; 20220801009@stu.cqu.edu.cn; dengming@cqu.edu.cn).

Digital Object Identifier 10.1109/JPHOT.2022.3230503

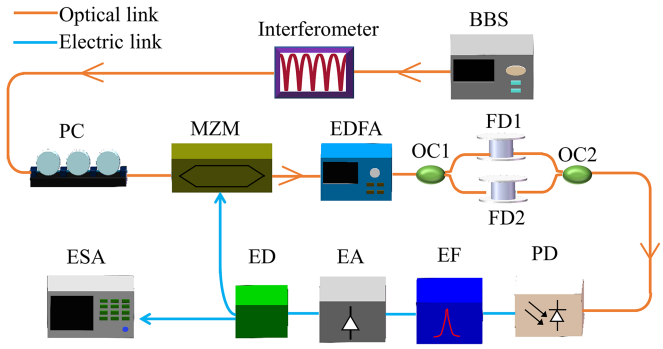

Fig. 1. Measurement system based on dual-loop OEO and fiber interferometer. BBS, broadband source; PC, polarization controller; MZM, Mach–Zehnder modulator; EDFA, erbium-doped fiber amplifier; OC, optical coupler; FD, fiber disc; PD, photodetector; EF, electrical filter; EA, electrical amplifier; ED, electrical divider; ESA, electrical spectrum analyzer.

which has the ability to achieve high reliability and precision [18], [19]. Recently, Sun et al. adopted the OEO in series with the MF-coated etched FBG for the magnetic field measurement, displaying the frequency sensitivity of 163 Hz/mT in the range of 5–10 mT [20]. However, the measurement range is relatively small because of poor corrosion uniformity of the FBG.

In this work, we experimentally demonstrate a RF-assisted Sagnac interferometer with the MF clad tapered fiber as the sensing probe used for high-precision magnetic field measurement. Firstly, according the sensing principles of the OEO, the effect of the birefringence on the mapping relation-ship between the FSR of the interference spectra and the oscillation frequency in the microwave domain is numerically analyzed, confirming the feasibility of the proposed scheme for high-precision magnetic field measurement. Next, the effect of the waist diameter of the tapered fiber on the fiber mode field distribution and birefringence characteristics is analyzed by the finite element method (FEM). The theoretical results suggest that the smaller the waist diameter, the stronger the evanescent field and the larger the mode birefringence. Given to the simulation, we prepare the tapered fiber with the waist diameter of ~7.5 μm, and adopt the proposed system to carry out the magnetic field measurement. The experimental results show the maximum magnetic field sensitivities of 159.4 Hz/mT in the range of 8.48–27.83 mT, and 350.8 Hz/mT in the range of 0–5.14 mT, corresponding to the light wave vector parallel and perpendicular the magnetic field, respectively. Finally, it should be pointed out that the birefringence and the measurement sensitivity can be further improved by introducing asymmetric structures or light field.

II. Method and Principles

The designed dual-loop OEO measurement system based on the fiber interferometer is shown in Fig. 1. The light emitted from a broadband source (BBS) is firstly segmented by a sine function after passing through a fiber interferometer, and then the sinusoidal-shaped light is injected into a Mach–Zehnder modulator (MZM) for the carrier intensity modulation after going through a polarization controller (PC), which is used to adjust the modulation efficiency and output power of the MZM. Subsequently, the intensity-modulated beam is amplified via an erbium-doped fiber amplifier (EDFA), and fed into a photodetector (PD) to realize the conversion of optical signals to electrical signals after passing through a set of time-delay devices consisting of two optical couplers (OC1 and OC2) and two single-mode fiber discs (FD1 and FD2). Next, the created electric signals are filtered and amplified in turn by an electrical filter (EF) and an electrical amplifier (EA). The later signals flow is divided into two paths through an electrical divider (ED), where one path is coupled back to the MZM to form the OEO loop, and the other path is directly sent into an electrical spectrum analyzer (ESA) to observe and record the frequency information. Because the fiber interferometer, as a sensing probe, can sense the change in the external physical quantity (magnetic field), causing the variation of free spectral range (FSR) in the optical domain, which leads to the frequency shift of the OEO in the electrical domain. As a result, we can establish the functional relationship between the oscillation frequency drift and magnetic field to characterize the external magnetic field.

The *N*th harmonic frequency of the dual-loop OEO can be expressed as [21]

$$f_N = N \cdot \mathrm{FSR_d} = \frac{1}{D_e \cdot L_{\cdot e} \mathrm{FSR_s}} \tag{1}$$

Where D_e and L_e are the equivalent dispersion coefficient and optoelectronic hybrid link length of the dual-loop OEO, respectively. N denotes the integer, and $\mathrm{FSR_S}$ is wavelength interval between adjacent wave peaks/valleys of the interferometer. In the configuration of dual-loop OEO, there are two sets of dispersion modules in parallel, which can be regarded as two independent single-loop OEO and FSR can be described as the following (2). According to the Vernier effect [22], the $\mathrm{FSR_d}$ of dual-loop OEO can be defined as the following (3).

$$\mathrm{FSR}_i = \frac{1}{\tau_i^t} = \frac{1}{\tau_i^e + \tau_i^o} = \frac{c}{nL_i} \quad (i = 1, 2) \tag{2}$$

$$\mathrm{FSR_d} = \frac{\mathrm{FSR_1} \times \mathrm{FSR_2}}{|\mathrm{FSR_1} - \mathrm{FSR_2}|} \tag{3}$$

where τ_i^t is total time delay of the optoelectronic link, including the electrical (τ_i^e) and optical (τ_i^o) link time delay. n = 1.45 is the RI of fiber core, and c is the light speed in vacuum, as well as L_i is the equivalent length of the *i*th single-loop OEO.

Given to the merits of the tapered fiber including strong evanescent field, easy preparation and small volume, we adopt the tapered fiber coated with the MF as the fiber magnetic field probe, as shown in Fig. 2(a). The sensing head is embedded in a capillary filled with the MF, whose axial direction is parallel to the fiber axis and two ends are sealed with UV glue. The simulated optical field distribution near the fiber taper and waist regions using the beam propagation method (BPM) in the RSoft software is drawn in Fig. 2(b). Note that the refractive indexes (RIs) of the fiber core, cladding and MF are 1.450, 1.444 and 1.400, respectively. From the monitor value of the normalized intensity in Fig. 2(c), the more energy leaks from the fiber core to the cladding as the fiber taper becomes thin, and the optical loss has maximum value in the waist region, which can strongly interact with the MF to cause the birefringence change between two orthogonally polarized core modes (Fig. 2(d) and (e)) under external magnetic field. Note that the mode field distributions

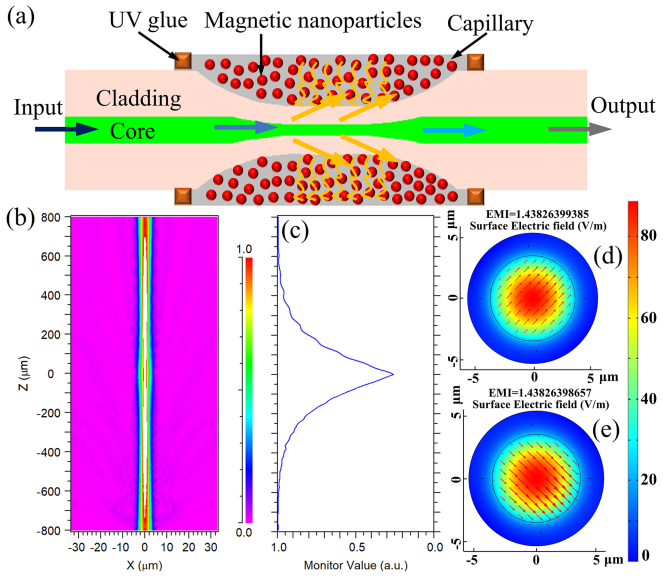

Fig. 2. (a) Schematic diagram of the tapered fiber magnetic field sensor, (b) Light field distribution and (c) normalized intensity near the fiber taper and waist regions, as well as the mode field distributions (d) and (e).

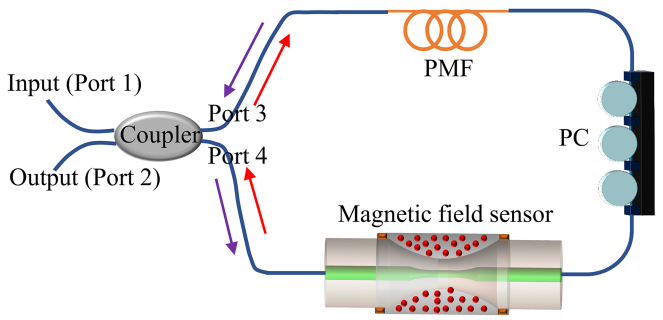

Fig. 3. Sagnac interferometer with taper-based magnetic field sensing head.

in Fig. 2(d) and (e) are derived from the simulated result in the waist section with the diameter of 7.5 μm at the magnetic field of 10 mT according to the model in Fig. 13(d-2), showing the mode birefringence of 7.28×10^{-9}.

As a result, Sagnac interferometer, as a kind of carrier of the above tapered fiber magnetic field probe, is a typical sensing configuration that can measure the magnetic field through the birefringence changes induced by the external magnetic field, as presented in Fig. 3. It consists of a 2 × 2 fiber coupler, a segment of polarization-maintaining fiber (PMF), a PC, and the above fiber magnetic field probe. The input light from port 1 is divided into the clockwise and counterclockwise transmission through ports 3 and 4, and the output light from port 2 carries an interference pattern derived from the phase difference between the fast and slow axes, whose transmission spectrum and FSR can be depicted as the following (4) and (5) [23], [24], respectively.

$$\mathrm{T} = \frac{1}{2}(1 + \cos(\varphi_{\mathrm{PMF}} + \varphi_{\mathrm{MF}})) \tag{4}$$

$$\mathrm{FSR_S} = \frac{\lambda^2}{B_{\mathrm{PMF}} L_{\mathrm{PMF}} + B_{\mathrm{MF}} L_{\mathrm{MF}}} \tag{5}$$

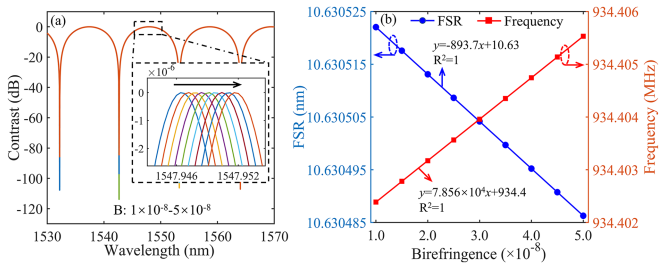

Fig. 4. (a) The simulated spectra response, (b) FSR and oscillation frequency shift for B changing from 1×10^{-8} to 5×10^{-8}.

where $\varphi_{\mathrm{PMF}} = 2\pi B_{\mathrm{PMF}} L_{\mathrm{PMF}}/\lambda$ and $\varphi_{\mathrm{MF}} = 2\pi B_{\mathrm{MF}} L_{\mathrm{MF}}/\lambda$, where B_{PMF} and L_{PMF}, B_{MF} and L_{MF} are the birefringence and length of the PMF and tapered fiber magnetic field probe, respectively.

According to the above (1) and (5), the Nth oscillation frequency of the OEO can be deduced as the following (6). When the external magnetic field is applied on the MF, it causes the birefringence change with ΔB_{MF} of the MF, resulting in the FSR variation of the Sagnac interferometer, so the new oscillation frequency of the OEO can be described as the following (7). Therefore, the relationship between the frequency shift of the OEO and the birefringence change can be built to characterize the external magnetic field, as shown in the (8).

$$f_N = \frac{B_{\mathrm{PMF}} L_{\mathrm{PMF}} + B_{\mathrm{MF}} L_{\mathrm{MF}}}{D_e \cdot L_e \cdot \lambda^2} \tag{6}$$

$$f'_N = \frac{B_{\mathrm{PMF}} L_{\mathrm{PMF}} + (B_{\mathrm{MF}} + \Delta B_{\mathrm{MF}}) L_{\mathrm{MF}}}{D_e \cdot L_e \cdot \lambda^2} \tag{7}$$

$$\Delta f = f'_N - f_N = \frac{\Delta B_{\mathrm{MF}} L_{\mathrm{MF}}}{D_e \cdot L_e \cdot \lambda^2} \tag{8}$$

Firstly, we simulate the spectral response of the Sagnac interferometer under different birefringence change, as shown in Fig. 4(a). The set parameters are as follows: $L_{\mathrm{PMF}} = 100$ cm, $B_{\mathrm{PMF}} = 2.26 \times 10^{-4}$, and $L_{\mathrm{MF}} = 19$ mm. When the birefringence (B) varies from 1×10^{-8} to 5×10^{-8}, the spectra create the redshift according to the (4), causing the corresponding changes in the FSR according to the (5) as shown in Fig. 4(b). The FSR varies between 10.630485 and 10.630525 nm with a fitting coefficient of -893.7 nm/B (Note that the unit nm/B is the FSR shift caused by the unit birefringence change) in the calculated birefringence, which results in the FSR changes not being distinguished by the spectrometer due to the minimum resolution of 20 pm. Given to the high resolution of the ESA with ~Hz magnitude, we convert the FSR changes of the interferometer in optical domain to the frequency shift in the microwave domain by the proposed RF-assisted scheme (Fig. 1) according to the (6), showing the fitting sensitivity of 7.856×10^4 MHz/B (Note that the unit MHz/B is the frequency shift caused by the unit birefringence change). In addition, compared to the slow scanning speed of the spectrometer, the OEO, as a kind of optoelectronic hybrid link, has high-speed digital processing device, which can achieve rapid signal response with high integration speed.

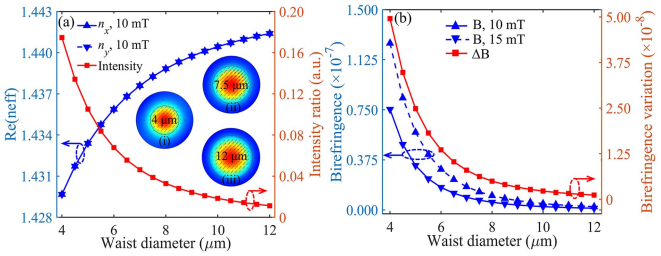

Fig. 5. Effect of the waist diameter on the (a) Re(neff) and evanescent field intensity ratio, and (b) birefringence and birefringence variation.

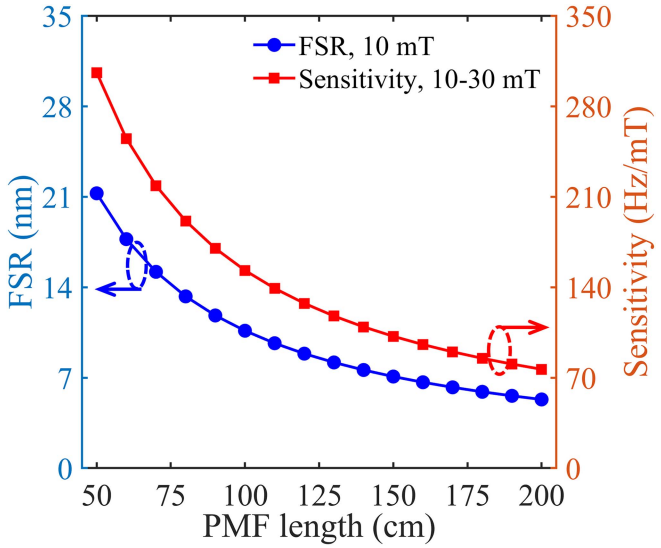

Fig. 6. Effect of the PMF length on the interferometer FSR and frequency sensitivity.

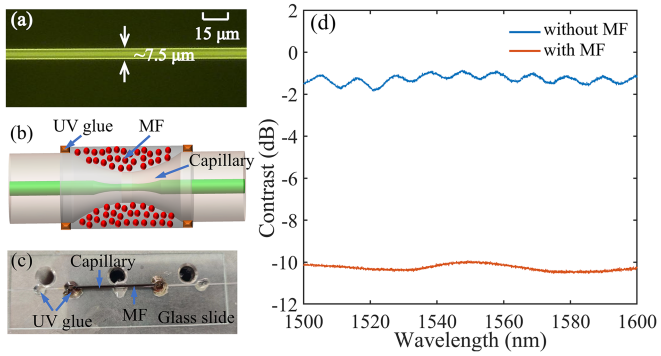

Fig. 7. (a) Micrograph of the prepared tapered fiber, (b) sensor encapsulation diagram, (c) the packaged sample, and (d) spectra before and after filling with the MF.

The waist diameter of the tapered fiber has strong dependence on the fundamental mode characteristics. According to the model shown in Fig. 13(d-2), we numerically analyze the effect of the waist diameter on the effective refractive index (Re(neff)) and electric field distribution of the fundamental mode at the magnetic field of 10 mT, as shown in Fig. 5(a). (Note that the numerical simulation is obtained by the mode analysis of the wave optics module in the COMSOL Multiphysics software based on the three-component vector finite element method (FEM). The mesh features use predefined extremely fine triangular meshes, and the total degree of freedom is ∼260000, as well as the complete meshes consist of ∼37000 domain elements and ∼700 boundary elements.) It can be seen that the Re(neff) reduces as the waist diameter decreases in the range from 4 to 12 μm with a step of 0.5 μm, while the evanescent field intensity ratio increases, which illustrates that the more light field is leaked to the MF area, as plotted in insets (i), (ii) and (iii) corresponding to the waist diameter of 4, 7.5 and 12 μm, respectively. (Note that the diameter of the fiber core in the waist area is much smaller than that of the cladding, resulting in the light field not being confined to the fiber core well, so we ignore the fiber core. In fact, the tapered fiber cladding and the coated MF act as the waveguide for the light transmission. Here, the evanescent field intensity ratio is defined as the energy in the MF area divided by the total energy in the cladding and MF areas.) When the magnetic field is 10 and 15 mT, the birefringence (B) and birefringence variation (ΔB) with respect to the waist diameter is plotted in Fig. 5(b). The B and ΔB diminish with the increment of the waist diameter in the calculated range, illustrating the decrement of the magnetic field measurement sensitivity. To sum up, taking the evanescent field intensity and operability of the tapered fiber into the consideration, the waist diameter of 7.5 μm is selected in the subsequent experiment.

According to the sensing principles, the change in the interferometer FSR caused by the external magnetic field is transformed into the OEO frequency shift according to the (7). The FSR is closely associated with the polarization maintaining fiber (PMF) length, which can directly affect the frequency sensitivity of the OEO measurement system. Therefore, according to the model shown in Fig. 13(d-2), the Re(neff) differences between two orthogonally polarized fundamental modes are calculated at the magnetic field of 10 and 30 mT, respectively, being used to evaluate the frequency sensitivity according to the (8), as presented in Fig. 6. It can be noted that the FSR decreases from 21.26 to 5.32 nm, and frequency sensitivity damps from 305.99 to 76.5 Hz/mT with the increment of the PMF length in the range of 50–200 cm. Although the high magnetic field sensitivity can be obtained in the situation of large FSR, the large FSR has fewer taps in the gain bandwidth of the EDFA (∼35 nm), which will reduce the signal-to-noise ratio (SNR) of the OEO. As a result, the PMF with 100 cm length is chosen in the Sagnac interferometer.

III. Experimental Result and Discussion

Considering the fragility and operability of the tapered fiber, we prepare the tapered fiber with the waist diameter of ∼7.5 μm using the melting tapering technology in the experiment, whose micrograph near the waist area is shown in Fig. 7(a). Fig. 7(b) presents the encapsulation diagram of the magnetic field probe. Firstly, the fabricated tapered fiber is embedded in a capillary with the inner diameter of 1 mm and length of 30 mm, and then the MF is injected into the capillary through a needle. Finally, the both ends are sealed with the UV glue, and the packaged

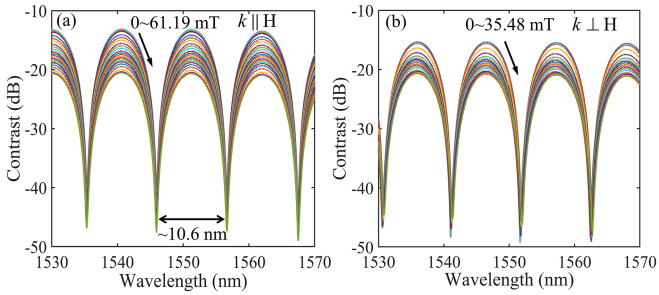

Fig. 8. Spectral response under different H for (a) $k \parallel$ H and (b) $k \perp$H.

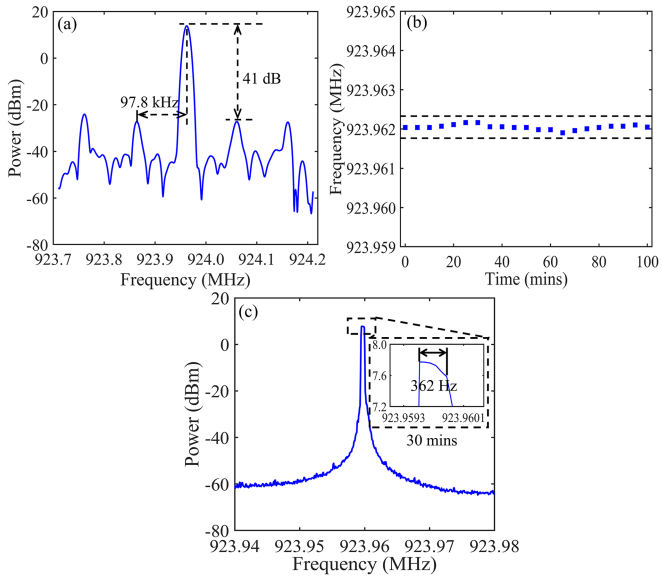

Fig. 9. (a) Electrical spectra at the center frequency of 923.96 MHz, (b) system stability in a 100 mins, and (c) frequency stability based on Max Hold mode in a 30 mins duration.

sample is shown in Fig. 7(c). Fig. 7(d) plots the spectra of the magnetic field sensor before and after filling with the MF. It can be seen that there is the mode interference with insignificant contrast before filling with the MF, which is due to the larger strength difference between the fundamental mode and the coupled low-order cladding mode. In addition, the spectral FSR is ∼10 nm, so the calculated sensing length of the tapered fiber is ∼19 mm according to the tapered modal interferometer theory. After filling with the MF, the whole spectrum drops by ∼9 dB because of the large absorption coefficient of the MF, enhancing the interaction between the optical field and MF. (Note that the adopted MF type is EMG605 with a particle diameter of 10 nm and black-brown appearance in the experiment, whose initial volume concentration and saturation magnetization is 3.9% and 22 mT at the temperature of 25 °C, respectively).

Firstly, the designed fiber taper-based magnetic field probe is placed in the Sagnac interferometer (Fig. 3) to evaluate the spectral response under different magnetic field. When the light wave vector (k) is parallel or perpendicular to the magnetic field (H), the effect of H on the transmission spectra are plotted in Fig. 8(a) and (b), respectively. Here, the used PMF length is 100 cm, so the FSR is ∼10.6 nm, which is almost equal to the theoretical value according to (5). Additionally, the spectral intensity is decayed by ∼7 dB with H increasing from 0 to 61.19 mT for $k \parallel$ H in Fig. 8(a), and lowered by ∼5 dB as H expands from 0 to 35.48 mT for $k \perp$H in Fig. 8(b), which is due to the increment of the absorption coefficient of the MF with H enlarging. It is worth noting that the entire spectra have no significant drift because of little change in the mode birefringence induced by the MF under the applied magnetic field. Another important reason is the minimum resolution limit (∼20 pm) of the used spectral analyzer, which is the inherent defect of the spectral detection method, resulting in low measurement accuracy.

In order to overcome low resolution of the spectrometer and achieve high-precision magnetic field measurement, we utilize the proposed system (Fig. 1) to characterize the external magnetic field by mapping the optical FSR change of the Sagnac interferometer to the oscillation frequency shift in the microwave domain. In our configuration, the wavelength range emitted from the BBS (VASS-C-Er-B-17-GF) is from 1535 to 1565 nm. The bandwidth and half-wave voltage of the MZM (TDKH1.5-10PDADC) are 10 GHz and 6 V. The PD (CETC GD45220R) has a 15 GHz bandwidth. The center frequency and bandwidth of the EF (Spectrum C942.5-40-6SS) are 940 MHz and 40 MHz. The dispersion elements consist of two parallel fiber discs (FDs) to offer initial time delay, including the FD1 with a length of 3 km and the FD2 with a length of 5 km. It can be treated as two independent single-loop OEO to generate two sets of harmonic frequency spectra with the theoretically calculated FSRs of ∼68.97 and ∼41.38 kHz according to the (2), respectively. As a result, the estimated electrical FSR derived from the dual-loop OEO is 103.44 kHz according to (3).

Fig. 9(a) shows the measured electrical spectrum with the center frequency of 923.96 MHz. The bandwidth and resolution are set to 500 kHz and 1 kHz in the experiment. It can be seen that there is the mode spacing of 97.8 kHz, which is nearly the same as the theoretical value (103.44 kHz). In addition, the side-mode suppression ration (SSR) of the frequency spectrum is up to 41 dB, ensuring good measurement accuracy. Fig. 9(b) describes the OEO system stability test. The corresponding spectra are recorded every 5 minutes for 100 minutes duration. The maximum frequency disturbance error is within ±130 Hz. In addition, we further assess the frequency stability of the dual-loop OEO system at the center frequency of 923.96 MHz by setting the Max Hold mode of the ESA as shown in Fig. 9(c). It can record the maximum frequency drift in a duration time. Here, the frequency span and resolution are set to 40 kHz and 100 Hz. It can be seen that maximum frequency shake is 362 Hz within 30 mins duration time, which is attributed to possible external environment fluctuation (e.g., temperature and vibration). It can be weaken by the thermostatic and vibration isolation devices or phase compensation methods [25].

Next, the magnetic field response adopting the dual-loop OEO system is evaluated. Note that the bandwidth and resolution of the ESA are set to 100 kHz and 1 kHz. When the light wave vector is parallel $(k \parallel \mathrm{H})$ and perpendicular $(k \perp \mathrm{H})$to the magnetic field, the effect of the magnetic field on the frequency spectra is drawn in Fig .10(a) and (c), respectively. Specifically,

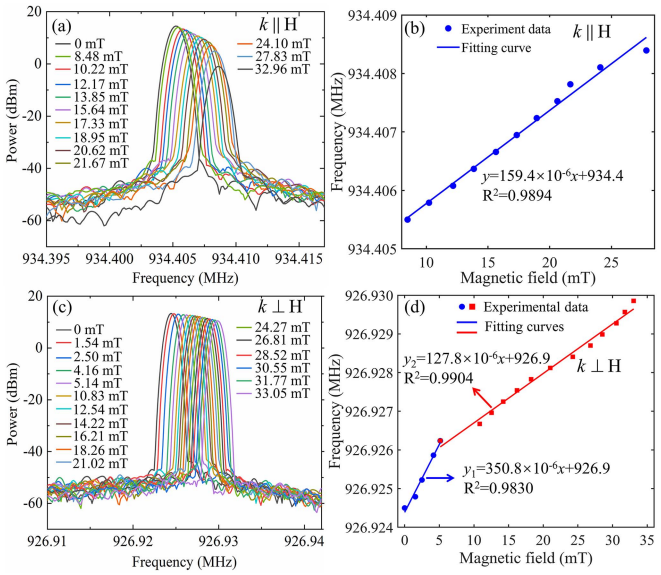

Fig. 10. Frequency response under different H for (a) $k \parallel$ H and (c) $k \perp$H, as well as the oscillation frequency with respect to H for (b) $k \parallel$ H and (d) $k \perp$H.

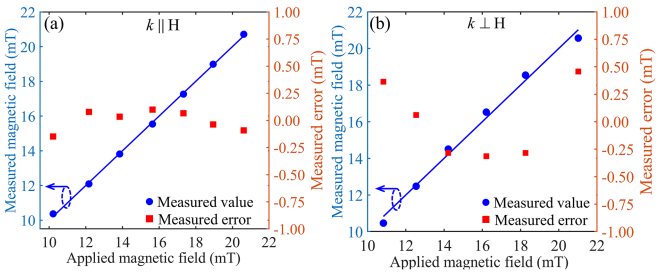

Fig. 11. Measured errors for (a) $k \parallel$ H and (b) $k \perp$H.

the oscillation frequency of the OEO shifts from 934.405210 to 934.408683 MHz with the increment of H from 0 to 32.96 mT in Fig. 10(a), from 926.924500 to 926.929855 MHz with the increment of H from 0 to 33.05 mT in Fig. 10(c). It needs to be pointed out that the maximum measurement range is limited by two aspects, where one is that the RI of the MF tends to the saturation when H>30 mT (as shown in Fig. 12). The other is that the absorption coefficient of the MF enlarges with H increasing, leading to the signal-to-noise ratio (SNR) reduction of the OEO and even the disappearance of the oscillation signal. The corresponding linear fitting curves between the oscillation frequency and magnetic field for $k \parallel$ H and $k \perp$H are plotted in Fig. 10(b) and (d), respectively. In Fig. 10(b), the magnetic field sensitivity of 159.4 Hz/mT with the R-square of 0.9894 is obtained in the range of 8.48-27.83 mT for $k \parallel$ H. In Fig. 10(d), the magnetic field sensitivities of 350.8 Hz/mT with the R-square of 0.9830 and 127.8 Hz/mT with the R-square of 0.9904 are acquired in the ranges of 0-5.14 mT and 5.14-33.05 mT for $k \perp$H , respectively. It needs to be noted that the detailed explanations to the above results are given in the following numerical analysis (Figs. 12 –16).

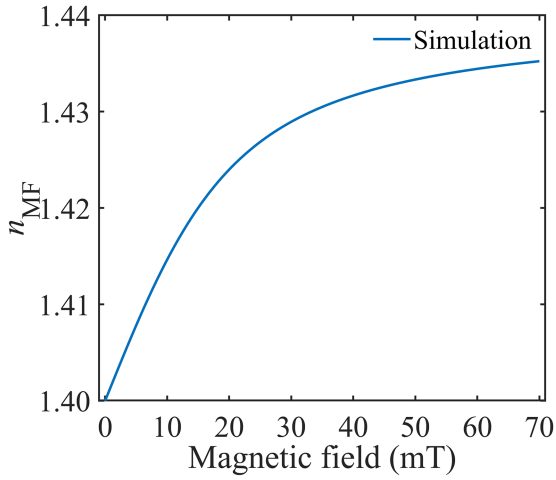

Fig. 12. Relationship between the simulated RI of MF and H.

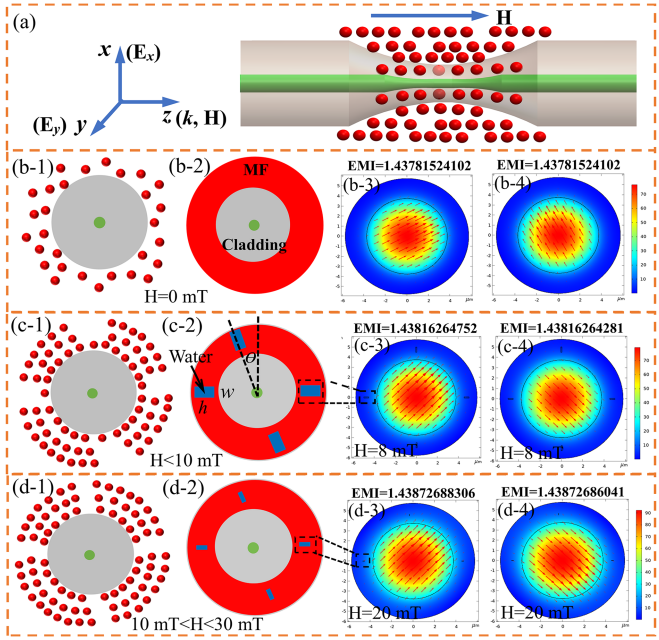

Fig. 13. (a) Spatial relationship between k and H with the insets showing the magnetic nanoparticles distribution, the simulated models, and electric field distributions as plotted in (b-1)-(b-4), (c-1)-(c-4), and (d-1)-(d-4) due to H changing in the ranges of 0 mT, 0-10 mT, and 10-30 mT, respectively.

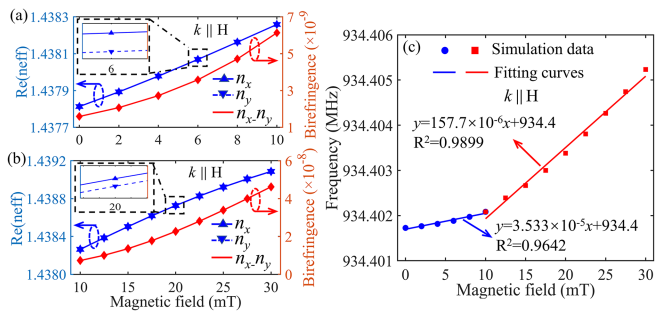

Fig. 14. Curves of the Re(neff) and birefringence in relation to H in the ranges of (a) 0-10 mT and (b) 10-30 mT, as well as (c) Relationship between the frequency and H.

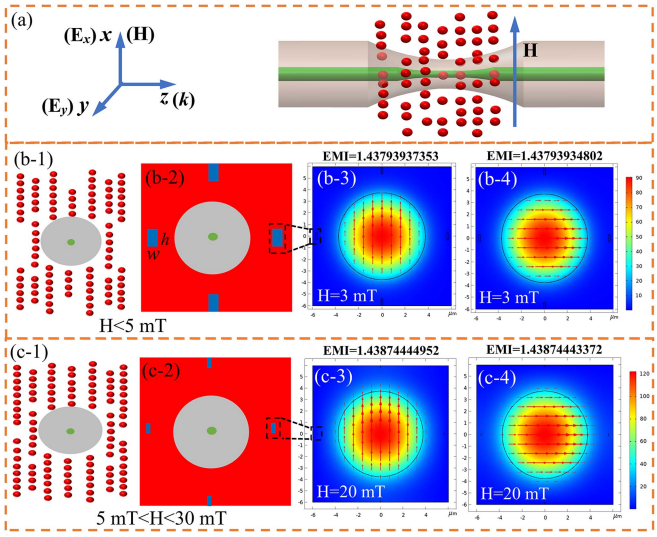

Fig. 15. (a) Spatial relationship between k and H with the insets showing the magnetic nanoparticles distribution, the simulated models, and electric field distributions as plotted in (b-1)-(b-4), and (c-1)-(c-4) due to H changing in the ranges of 0-5 mT, and 5-30 mT, respectively.

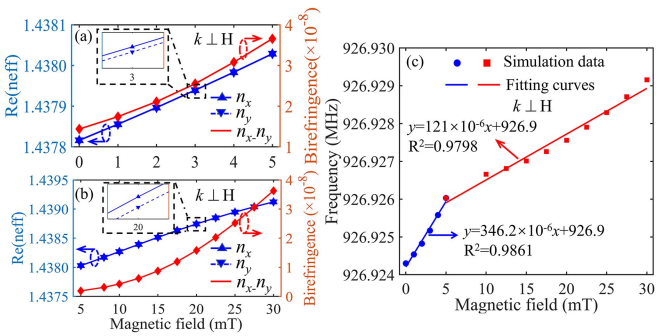

Fig. 16. Curves of the Re(neff) and birefringence with respect to H for H changing in the ranges of (a) 0-5 mT and (b) 5-30 mT, as well as (c) Relationship between frequency and H.

Further, the magnetic field measurement errors of the designed OEO scheme are evaluated as plotted in Fig. 11. The measurement errors are defined as the difference between the applied magnetic field and the measured values obtained from the linear sensitivity fitting relationship within the specified magnetic field range. Fig. 11(a) and (b) represent the magnetic field measurement errors for $k \parallel$ H and $k \perp$H, which reveals the maximum measurement errors of within $\pm$0.15 mT (Fig. 11(a)) and $\pm$0.46 mT (Fig. 11(b)) in the ranges of 10.22-20.62 mT and 10.83-21.02 mT, respectively. The proposed sensing scheme shows a certain potential in the precise magnetic field measurement fields.

In order to explain the above frequency response for $k \parallel$ H and $k \perp$H better, we construct possible simulation models. The RI of the MF is strongly dependent on many factors, such as magnetic nanoparticles, base liquid, concentration, Brownian motion closely related to temperature, external magnetic field and optical capture, which can be described by Langevin function as shown in (9) [26]. The simulated parameters are as follows: $n_s = 1.44$, $n_b = 1.40$, $H_c = 1$ Oe, $\alpha = 0.3$, T = 25°C. Fig. 12 draws the curve on the RI of the MF in relation to the magnetic field in the simulation.

$$n_{MF} = (n_s - n_b)[\coth\left(\alpha\frac{H - H_{c,n}}{T}\right) - \frac{T}{\alpha(H - H_{c,n})}] + n_b \tag{9}$$

where H and $H_{c,n}$ are external and critical magnetic field intensity. n_s and n_b represent the saturated and initial RI of the MF. α and T denote the fitting parameter and temperature.

When light wave vector is parallel to magnetic field ($k \parallel$ H), the x-polarized (E_x) and y-polarized (E_y) components of the fundamental mode are both perpendicular to the magnetic field ($E_x \perp$H and $E_y \perp$H), as drawn in Fig. 13(a). Taking the waist cross-section of the tapered fiber as an example, the distribution characteristics of the magnetic nanoparticles are analyzed. When H is not applied to the MF, the magnetic nanoparticles are randomly distributed near the waist region, and the simplified model is shown in Fig. 13(b-1) and (b-2). The x- and y-polarized distributions of the fundamental modes are plotted in Fig. 13(b-3) and (b-4), showing the birefringence difference with almost zero value. When H is applied to the MF, the magnetic nanoparticles will form the magnetic chains along the magnetic field direction, whose RI is described by (9), and the magnetic chain gaps are the water-based liquid with the RI of 1.333, as shown in Fig. 13(c-1) and (c-2), (d-1) and (d-2). When H changes in the ranges of 0-10 mT and 10-30 mT, the simulated models are shown in Fig. 13(c-2) and (d-2) (Note that the red areas are on behalf of the MF, and the water-based areas are represented by four simplified blue rectangles with the height of h and width of w. In addition, an angle θ is used to adjust the possible chain direction). In Fig. 13(c-2), when H varies between 0 and 10 mT, the initial water-based areas have relatively large areas with the assumed parameters of $w = 0.1$ μm, $h = 0.5$ μm, and $\theta = 0.15°$. The corresponding x- and y-polarized distributions are presented in Fig. 13(c-3) and (c-4) for H = 8 mT, showing the birefringence of 4.71×10^{-9}. As H expands from 10 to 30 mT, the formed magnetic chains increase and the water-based areas reduce, so the simulated water-based areas with $w = 0.01$ μm, $h = 0.2$ μm, and $\theta = 4.5°$are set in Fig. 13(d-2). For H = 20 mT, the x- and y-polarized birefringence difference is 2.26×10^{-8}, as shown in Fig. 13(d-3) and (d-4). When H>30 mT, the water-based areas decrease further, and the magnetic chains gradually reach the saturation, just like the model in Fig. 13(b-2), resulting in the birefringence damping again.

In order to numerically illustrate the effect of the magnetic chains under different H on the optical characteristic parameters for $k \parallel$ H, according to the models shown in Fig. 13(c-2) and (d-2), we firstly analyze the relationships between H and the mode birefringence for $k \parallel$ Hwhen H varies in the ranges of 0-10 mT (Fig. 14(a)) and 10-30 mT (Fig. 14(b)), respectively. It can be seen that the Re(neff) of x- and y-polarized fundamental modes enlarges, corresponding to the birefringence increasing from 1.59×10^{-9} to 6.13×10^{-9} (Fig. 14(a)), and 7.28×10^{-9} to 4.62×10^{-8} (Fig. 14(b)) for H expanding in the simulated ranges, respectively. According to (8), the oscillation frequency

TABLE I
PERFORMANCE COMPARISON BETWEEN THE PROPOSED AND THE REPORTED SENSING SCHEMES

Scheme	Sensitivity	Range	Sensing head	Size	Ref
OEO with MA-FBG-FP and FBG-FP filters	-384 MHz/mT	2-7 mT	MA-FBG-FP and FBG-FP	ϕ 0.5×20 mm	[18]
OEO with MZI and GMM	1.33 MHz/mT	20.9-50.8 mT	MZI in combination with GMM	4×8×40 mm	[19]
OEO with etched FBG coated with MF	163 Hz/mT	5-10 mT	Etched FBG coated with MF	-	[20]
OEO with MA-FBG	2.5 kHz/mT	24-76 mT	MA-FBG	50×12×8 mm	[25]
Ours	350.8 Hz/mT	0-5.14 mT	Tapered fiber coated with MF	ϕ 1×30 mm	-
	159.4 Hz/mT	8.48-27.83 mT			

shift of the OEO with respect to H is shown in Fig. 14(c), revealing the frequency sensitivities of 35.33 Hz/mT with the R-square of 0.9642 in the range of 0-10 mT, and 157.7 Hz/mT with the R-square of 0.9899 in the range of 10-30 mT, which is the nearly same as the experimental results (159.4 Hz/mT in the 8.48-27.83 mT, Fig. 10(b)). It can be noted that the measurement sensitivity in the range of 0-10 mT is less than that in the range of 10-30 mT. which is due to the formation of the longer magnetic chains requiring a certain accumulation of the magnetic field [27]. When H is less than 10 mT, the formed short magnetic chains have little effect on the birefringence of the fundamental mode, leading to an inconspicuous frequency spectra shift (Fig. 10(a)) and low measurement sensitivity. As the magnetic field enlarges (H>10 mT), the magnetic chains length increases further, resulting in relatively large mode birefringence and high measurement sensitivity.

Similarly, when light wave vector is perpendicular to magnetic field ($k\perp$H), in other words, the *x*-polarized component is parallel to H ($\mathrm{E}_x \parallel$ H) and *y*-polarized component is perpendicular to H ($\mathrm{E}_y\perp$H), as shown in Fig. 15(a). When H changes in the range of 0-5 mT, the initial water-based areas possess a relatively large size with $w = 0.14$ μm and $L = 0.6$ μm in Fig. 15(b-1) and (b-2), showing the mode birefringence of 2.55×10^{-8} for H = 3 mT in Fig. 15(b-3) and (b-4). When H increases in the range of 5-30 mT, the water-based areas decrease with the size of $w = 0.01$ μm and $L = 0.2$ μm in Fig. 15(c-1) and (c-2), showing the mode birefringence of 1.58×10^{-8} for H = 20 mT in Fig. 15(c-3) and (c-4). When H>30 mT, the water-based areas reduce further, and the simulated model is the same as that shown in Fig. 13(b-2).

According to the models shown in Fig. 15(b-2) and (c-2), the effect of H on the mode birefringence for $k\perp$H is studied when H changes in the ranges of 0-5 mT (Fig. 16(a)) and 5-30 mT (Fig. 16(b)), respectively. It can be found that the Re(neff) increases, corresponding to the mode birefringence expanding from 1.44×10^{-8} to 3.66×10^{-8} (Fig. 16(a)), and from 1.92×10^{-9} to 3.63×10^{-8} (Fig. 16(b)) for H increasing in the simulated ranges, respectively. According to (8), Fig. 16(c) depicts the oscillation frequency shift in relation to H, obtaining the frequency sensitivities of 346.2 Hz/mT with the R-square of 0.9861 in the range of 0-5 mT, and 121 Hz/mT with the R-square of 0.9798 in the range of 5-30 mT, which is the nearly same as the experimental results (350.8 and 127.8 Hz/mT in the ranges of 0-5.14 and 5.14-33.05 mT in Fig. 10(d)). In addition, it is important to point out that the original frequency sensitivity for $k\perp$H (346.2 Hz/mT in the range of 0-5 mT, Fig. 16(c)) is obviously higher than that for $k \parallel$ H (35.33 Hz/mT in the range of 0-10 mT, Fig. 14(c)) The reason is that the light field vectors (E_x andE_y) are asymmetrical to H for $k\perp$H ($\mathrm{E}_x \parallel$ H and $\mathrm{E}_y\perp$H) compared to the symmetrical situation for $k \parallel$ H ($\mathrm{E}_x\perp$Hand $\mathrm{E}_y\perp$H), so a larger initial mode birefringence is introduced for$k\perp$H due to the asymmetrical optical field. With the magnetic field enlarging further, the magnetic chains tend to the saturation and the asymmetric optical field effect is weakened, causing the sensitivity for $k\perp$H (121 Hz/mT in the range of 5-30 mT, Fig. 16(c)) being reduced and nearly consistent with that for $k \parallel$ H (157.7 Hz/mT in the range of 10-30 mT, Fig. 14(c)). Besides, the relatively low fitting accuracy of the sensitivity is mainly due to a certain nonlinear birefringence with the increment of magnetic field.

Finally, we make a performance comparison (sensitivity, sensing range and size) between the proposed and the reported OEO schemes as listed in Table I. The magnetic field sensors include the OEO in combination with the magnetostrictive alloy-fiber Bragg grating-Fabry Perot (MA-FBG-FP) and FBG-FP filters [18], Mach-Zehnder interferometer (MZI) and giant magnetostrictive material (GMM) [19], the etched FBG coated with MF [20], and MA-FBG [25]. Although the sensors in Refs. [18], [19] and [25] can achieve high measurement sensitivity, they have bulky size, limiting their potential applications in the narrow space. In addition, it can be seen that our proposed sensor has wide dynamic measurement range compared with those in Refs. [18] and [20].

IV. CONCLUSION

In this work, a high-precision magnetic field measurement system is experimentally proved by utilizing the OEO in combination with the Sagnac interferometer, where the MF-coated tapered fiber as the sensing probe is inserted in the Sagnac loop. Firstly, the feasibility of the proposed scheme is verified in theory based on the sensing principle of converting the optical FSR change to the oscillation frequency shift in the microwave domain. Next, the effect of the waist diameter of the tapered fiber on the mode field characteristics (evanescent field intensity and birefringence) is numerically analyzed by the finite element

method, which suggests that the smaller the waist diameter, the stronger the evanescent field and the larger the mode birefringence. According to the simulation results, we fabricate the tapered fiber with the waist diameter of $\sim$7.5 μm and perform the magnetic field measurement experiment using the proposed system. The experimental results reveal themaximum frequency sensitivities of 159.4 Hz/mT in the range of 8.48-27.83 mT for $k \parallel$ H , and 350.8 Hz/mT in the range of 0-5.14 mT for $k \perp$H, respectively, which shows a certain directionality of the magnetic field measurement. The proposed device has the virtues of easy preparation, simple operation, high accuracy and interrogation speed, providing some potential application in the fields of magnetic field measurement.

REFERENCES

[1] D. M. Lekidc, P. D. Mrsic, B. B. Erceg, C. V. Zeljkovic, N. S. Kitic, and P. R. Matic, "Generalized approach for fault detection in medium voltage distribution networks based on magnetic field measurement," *IEEE Trans. Power Del.*, vol. 35, no. 3, pp. 1189–1199, Jun. 2020.

[2] F. Nemec, D. Morgan, D. Gurnett, and D. Andrews, "Empirical model of the Martian dayside ionosphere: Effects of crustalmagnetic fields and solar ionizing flux at higher altitudes," *J. Geophysical Res. Space Phys.*, vol. 121, pp. 1760–1771, Feb. 2016.

[3] Y. M. Zhang, G. J. Zhang, Z. Zhang, Y. Zhang, and Y. Huang, "Effect of assisted transverse magnetic field on distortion behavior of thin-walled components in WEDM process," *Chin. J. Aeronaut.*, vol. 35, pp. 291–307, Feb. 2022.

[4] Y. Yin et al., "The influence of modulated magnetic field on light absorption in SERF atomic magnetometer," *Rev. Sci. Instrum.*, vol. 93, Jan. 2022, Art. no. 013001.

[5] Y. P. Miao et al., "Magnetic field tunability of optical microfiber taper integrated with ferrofluid," *Opt. Exp..*, vol. 21, pp. 29914–29920, Dec. 2013.

[6] Y. Zhao, D. Wu, and R. Q. Lv, "Magnetic field sensor based on photonic crystal fiber taper coated with ferrofluid," *IEEE Photon. Technol. Lett.*, vol. 27, no. 1, pp. 26–29, Jan. 2015.

[7] P. Zu et al., "Temperature-insensitive magnetic field sensor based on nanoparticle magnetic fluid and photonic crystal fiber," *IEEE Photon. J.*, vol. 4, no. 2, pp. 491–498, Apr. 2012.

[8] J. F. Lin, J. J. Sheu, and M. Z. Lee, "Measurement of birefringence and dichroism in magnetic fluid doped with silica microsphere," *IEEE Trans. Magn.*, vol. 50, no. 1, Jan. 2014, Art. no. 4003604.

[9] T. Liu, Y. Chen, Q. Han, and X. Lu, "Magnetic field sensor based on U-bent single-mode fiber and magnetic fluid," *IEEE Photon. J.*, vol. 6, no. 6, Dec. 2014, Art. no. 5300307.

[10] Z. J. Hao et al., "Dual-channel temperature-compensated vector magnetic field sensor based on lab-on-a-fiber-tip," *Opt. Exp.*, vol. 30, pp. 25208–25218, Jul. 2022.

[11] Y. X. Li, S. L. Pu, Z. J. Hao, S. K. Yan, Y. X. Zhang, and M. Lahoubi, "Vector magnetic field sensor based on U-bent single-mode fiber and magnetic fluid," *Opt. Exp.*, vol. 29, pp. 5236–5246, Feb. 2021.

[12] P. Zu et al., "Enhancement of the sensitivity of magneto-optical fiber sensor by magnifying the birefringence of magnetic fluid film with Loyt-Sagnac interferometer," *Sensor Actuators B-Chem.*, vol. 191, pp. 19–23, Feb. 2014.

[13] P. Zu et al., "Magneto-optic fiber Sagnac modulator based on magnetic fluids," *Opt. Lett.*, vol. 36, pp. 1425–1427, Apr. 2011.

[14] X. Q. Lei, J. J. Chen, F. Q. Shi, D. R. Chen, Z. J. Ren, and B. J. Peng, "Magnetic field fiber sensor based on the magneto-birefringence effect of magnetic fluid," *Opt. Commun.*, vol. 374, pp. 76–79, Sep. 2016.

[15] F. F. Wei et al., "Magnetic field sensor based on a combination of a microfiber coupler covered with magnetic fluid and a Sagnac loop," *Sci. Rep.*, vol. 7, Jul. 2017, Art. no. 4725.

[16] W. H. Wang, H. M. Zhang, B. Li, Z. Li, and Y. P. Miao, "Optical fiber magnetic field sensor based on birefringence in liquid core optical waveguide," *Opt. Fiber Technol.*, vol. 50, pp. 114–117, Jul. 2019.

[17] F. Zhang et al., "A magnetic field sensor based on birefringence effect in asymmetric four-hole fiber," *J. Lightw. Technol.*, vol. 40, no. 8, pp. 2594–2600, Apr. 2022.

[18] B. L. Wu et al., "Magnetic field sensor based on a dual-frequency optoelectronic oscillator using cascaded magnetostrictive alloy-fiber Bragg grating-Fabry Perot and fiber Bragg grating-Fabry Perot filters," *Opt. Exp.*, vol. 26, pp. 27628–27638, Oct. 2018.

[19] N. Zhang et al., "Temperature-insensitive magnetic field sensor based on an optoelectronic oscillator merging a Mach-Zehnder interferometer," *IEEE Sens. J.*, vol. 20, no. 13, pp. 7053–7059, Jul. 2020.

[20] W. Sun, X. Y. Liu, and M. Deng, "High-precision magnetic field sensor based on fiber Bragg grating and dual-loop optoelectronic oscillator," *Photon. Sensors*, vol. 12, Jun. 2022, Art. no. 220419.

[21] D. Ming, X. Y. Liu, D. Q. Feng, Y. X. Tang, and T. Zhu, "Trace copper detection using in-line optical fiber Mach-Zehnder interferometer combined with an optoelectronic oscillator," *Opt. Exp.*, vol. 29, pp. 23430–23438, Jul. 2021.

[22] Y. J. Cheng, Y. P. Wang, Z. X. Song, and J. Lei, "High-sensitivity optical fiber temperature sensor based on a dual-loop optoelectronic oscillator with the Vernier effect," *Opt. Exp.*, vol. 28, pp. 35264–35271, Nov. 2020.

[23] Y. Zhao, D. Wu, R. Q. Lv, and J. Li, "Magnetic field measurement based on the Sagnac interferometer with a ferrofluid-filled high-birefringence photonic crystal fiber," *IEEE Trans. Instrum. Meas.*, vol. 65, no. 6, pp. 1503–1507, Jun. 2016.

[24] D. H. Kim and J. U. Kang, "Sagnac loop interferometer based on polarization maintaining photonic crystal fiber with reduced temperature sensitivity," *Opt. Exp.*, vol. 12, pp. 4490–4495, Sep. 2004.

[25] D. Q. Feng, Y. Gao, T. Zhu, M. Deng, X. H. Zhang, and L. Kai, "High-precision temperature-compensated magnetic field sensor based on optoelectronic oscillator," *J. Lightw. Technol.*, vol. 39, no. 8, pp. 2559–2564, Apr. 2021.

[26] E. L. Wang, P. Cheng, J. Li, Q. Cheng, X. D. Zhou, and H. M. Jiang, "High-sensitivity temperature and magnetic sensor based on magnetic fluid and liquid ethanol filled micro-structured optical fiber," *Opt. Fiber Technol.*, vol. 55, Mar. 2020, Art. no. 102161.

[27] R. Q. Lv, Y. Zhao, N. Xu, and H. Li, "Research on the microstructure and transmission characteristics of magnetic fluids film based on the Monte Carlo method," *J. Magnetism Magn. Mater.*, vol. 337, pp. 23–28, Jul. 2013.